Processing–Property Interactions in Poly(vinylidene Fluoride). I. An Analysis of Melt Stress History in an Extensional Flow Geometry

B. KHOMAMI and A. J. McHUGH, *Department of Chemical Engineering, University of Illinois, Urbana, Illinois 61801*

Synopsis

A numerical and experimental analysis of the melt flow history of poly(vinylidene fluoride), PVF_2, in an extensional flow, film-processing geometry is presented. Numerical computations were carried out for both Newtonian and power law flow in an impinging channels die using a finite-element technique. Computations demonstrate that a strong extensional flow exists in the region from the stream impingement point to a distance about 0.75 D downstream where D is the channel height at the impingement point. Measurements of the stress fields using the technique of flow birefringence showed that in consequence of the changing flow kinematics from the stream impingement region to the downstream converging channels region, both the isochromatic and isoclinic patterns exhibit a pronounced axial positional dependence. Excellent qualitative and quantitative agreement was found between measured and calculated shear stress fields. However, large differences were exhibited between calculated and measured normal stress differences along the symmetry axis of flow. Results to be presented in a companion paper (Part II) demonstrate that the strong extensional flow which occurs in this geometry is sufficient to produce oriented, row-nucleated structures in the extruded PVF_2 films.

INTRODUCTION

Poly(vinylidene fluoride), PVF_2, is an interesting thermoplastic polymer which is known to exhibit at least four different crystalline modifications depending on its thermal and processing history.[1] The technological importance of this material stems largely from the piezoelectric properties exhibited by the β polymorph (form I) in which the unit cell is orthorhombic and the chain conformational state is the all-trans or extended, planar zigzag. Alternate observed crystalline forms are the α phase (form II) normally obtained by crystallization from the quiescent melt, in which the chain conformation is a sequence of slightly distorted trans and gauche states, the γ phase, with chains in the $T_3GT_3\bar{G}$ conformation, and the so-called δ phase, obtained by poling the α form in high electric fields. The β polymorph is generally obtained by hot drawing melt-crystallized films of the α material at temperatures in the neighborhood of 50–100°C. Since interconversions of the various polymorphs are readily induced by thermal and mechanical treatments either during or after crystallization, structure–processing interactions are more involved with this material than would generally be the case with the more conventional thermoplastics.

Since most studies of PVF_2 have focused on postcrystallization treatments or solid-state extrusion (or coextrusion) to produce the β phase,[2,3] relatively

little is known concerning the effects of stress-induced conformational changes in the melt state on the crystallization and processing behavior. The purpose of the present study has therefore been to carry out a complete analysis of the effects of melt flow history, and, in particular, extensional flows, on the oriented crystallization and subsequent α to β transformation behavior of PVF_2 films. Melt orientation has been achieved in a two-dimensional elongational flow using a die geometry discussed in an earlier publication.[4] Extruded films were subjected to various thermal and drawing histories and then fully characterized for both morphological and physical properties. In this article we wish to present the details of our computational and experimental analyses (through flow birefringence) of the stress and flow histories associated with melt flow in the die. Results of the morphology and property characterizations of the extruded films will be presented in a companion paper (Part II). We begin first with a general analysis of the relevant equations and a discussion of the calculated flow and stress field behavior.

GOVERNING FLOW EQUATIONS

Figure 1 shows a general schematic of the film die geometry which consists of two flow channels approaching at an angle, γ, to form a single converging wall downstream channel having an angle of convergence, α, as shown. For purposes of comparison, calculations were also carried out for a parallel wall downstream configuration in which case $\alpha = 0$. In an earlier paper[4] numerical solutions for Stokes flow in these geometries were obtained using a nonorthogonal transformation of variables to convert the system to a square grid geometry. Calculations showed that a strong extensional flow exists from the point of channel impingement to a distance downstream approximately $D/4$ where D is the channel height at the impingement point. Extensional gradients and total fluid strains also increased when the downstream channel converged. In the present study we are concerned with developing a more
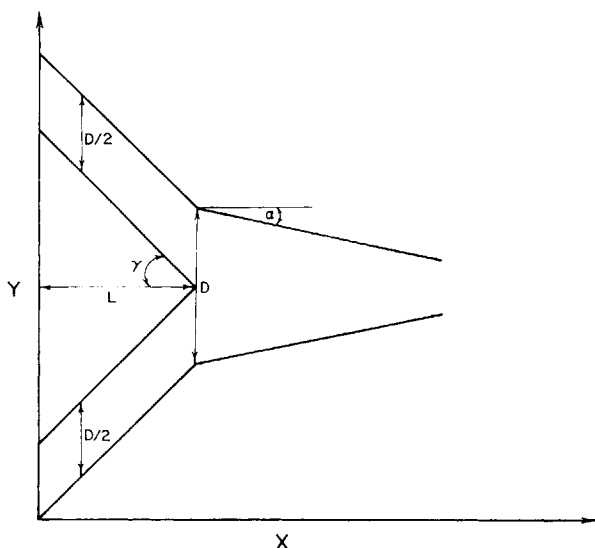

Fig. 1.   Schematic of die flow geometry and calculation coordinates.

exact numerical analysis of the flow and stress fields for comparison to experimental data. Thus we have developed a more general treatment based on a finite-element method which includes the effects of the nonlinear momentum terms in the equations of motion as well as non-Newtonian effects through use of a power law model.

The appropriate stress, continuity, and constitutive equations for the two-dimensional flow can be expressed in the following dimensionless forms,

$$u_i\frac{\partial u_j}{\partial x_i} = -\frac{\partial P}{\partial x_j} + \frac{1}{\mathrm{Re}}\frac{\partial \tau_{ij}}{\partial x_i} + \frac{1}{\mathrm{Fr}}g_j \quad j = 1,2 \tag{1}$$

$$\frac{\partial u_j}{\partial x_j} = 0 \tag{2}$$

$$\tau_{ij} = 2^{(n+1)/2}(\mathbf{d}\colon \mathbf{d})^{(n-1)/2}d_{ij} \tag{3}$$

where Re is the generalized Reynolds number for power law flow

$$\mathrm{Re} = \frac{D^n u_o^{2-n}}{m}\rho \tag{4}$$

in which m and n are the usual power law parameters,[5] ρ is density, and Fr is the Froude number. In these equations the standard summation convention is used and both indices have the range $i, j = 1, 2$ corresponding respectively to the dimensionless x or y coordinate. Velocity components, $u_x(x, y)$ and $u_y(x, y)$, have been nondimensionalized with respect to the average velocity at the bifurcation point, u_o, position variables with respect to the channel depth at the bifurcation point, D (see Fig. 1) and stress components, τ_{ij}, with respect to $m(u_o/D)^n$. The remaining nondimensionalizations for the isotropic pressure and gravity terms are standard[5] and the dimensionless (with respect to u_o/D) deformation rate tensor, d_{ij} is given by

$$d_{ij} = \frac{1}{2}\left(\frac{\partial u_i}{\partial x_j} + \frac{\partial u_j}{\partial x_i}\right) \tag{5}$$

For the boundary conditions, we assume that both the inlet and outlet positions are far enough from the channel insert for the corresponding flow fields to be fully developed. Thus at the inlet to the two channels the following will hold.
Upper branch:

$$u_x = 2\left(\frac{1 + 2n}{1 + n}\right)\left[1 - (4y - 8\tan\gamma - 3)^{1+1/n}\right] \tag{6a}$$

$$u_y = -(\tan\gamma)u_x \tag{6b}$$

Lower branch:

$$u_x = 2\left(\frac{1 + 2n}{1 + n}\right)\left[1 - (4y - 1)^{1 + 1/n}\right] \qquad (7a)$$

$$u_y = (\tan\gamma)u_x \qquad (7b)$$

while for the exit (assumed to be at 1.5 D from the insert)

$$u_x = \frac{\left(\dfrac{1 + 2n}{1 + n}\right)\cos\theta}{(1 - 3\tan\alpha)^{2 + 1/n}}\left[(1 - 3\tan\alpha)^{1 + 1/n} - (2y - 2\tan\gamma - 1)^{1 + 1/n}\right] \quad (8a)$$

$$u_y = -(\tan\theta)u_x \qquad (8b)$$

In these expressions

$$\theta = \arctan\left(\frac{1 - 2y + 2\tan\gamma}{3 - \cot\alpha}\right)$$

and L/D is taken as unity. Solutions to this equation set were generated numerically using a finite-element algorithm available in FIDAP.[6] Simulations were carried out over a range of Reynolds numbers for Newtonian and power law behavior for both converging and straight ($\alpha = 0$) downstream channel geometries. Mesh generation and solution strategies followed the usual logic[7,8] and complete details can be found in ref. 9.

NUMERICAL RESULTS

A range of flows corresponding to Reynolds numbers between 0.1 and 160 were simulated, and for Re < 90 in either geometry, secondary flows were found to be absent. Thus since velocity and stress fields scale with the nondimensionalizing parameters in this region, patterns in the dimensionless variables reflect the general behavior. A typical example to illustrate the nature of the velocity profile development for Newtonian flow in the converging wall geometry is shown in Figure 2. In this and all subsequent converging channel flows, $\gamma = 45°$, $\alpha = 11.25°$. The dimensionless centerline velocity is seen to rapidly increase from zero at the insert to a value of about 0.3 at the point where the profile becomes fully developed, after which one sees the expected pattern for converging flow. The pattern of profile development for the straight wall case was virtually identical except for the fully developed region where the constant shearing flow profile resulted. Figure 3 shows a comparison of the axial dependence of the centerline velocity for the two cases. The sudden jump in velocity at the impingement point is followed, in the straight channel, by a flat region corresponding to fully developed shearing flow, and, in the converging channel, by an S-shaped profile corresponding to the transition from the impinging-stream kinematics to converging flow kinematics. The centerline extensional gradient, $\partial u_x/\partial x$, from the slopes of these curves, decreases from a maximum value at the insert to either zero
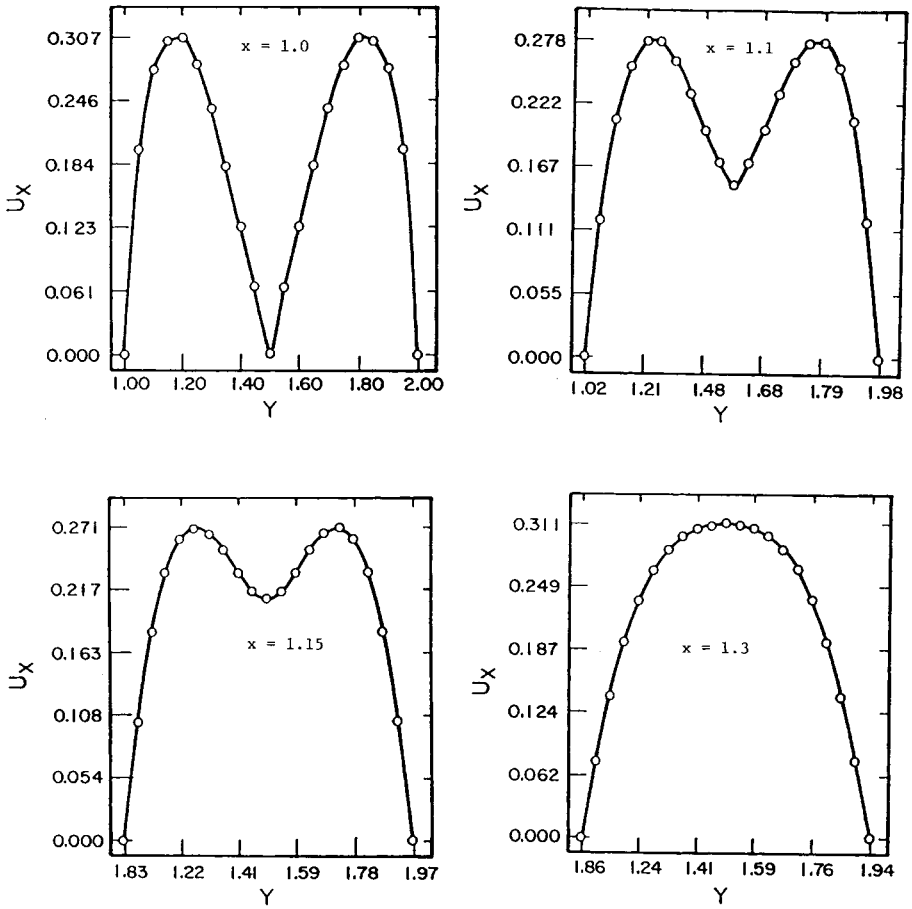
Fig. 2.   Dimensionless velocity profiles at various axial positions for Newtonian flow in the converging wall geometry. $\gamma = 45°$, $\alpha = 11.25°$.
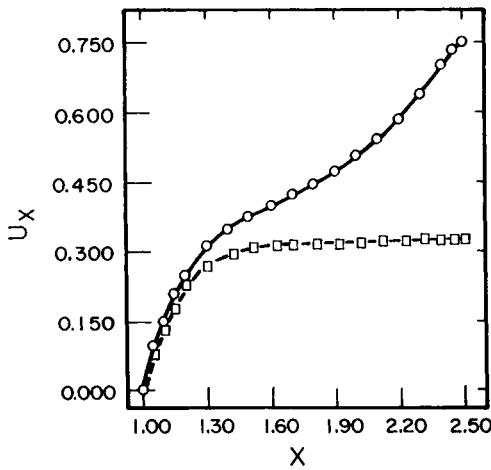

Fig. 3.   Comparison of centerline velocity axial dependence for Newtonian flow in (○) converging channel ($\gamma = 45°$, $\alpha = 11.25°$) and (□) straight channel geometries.
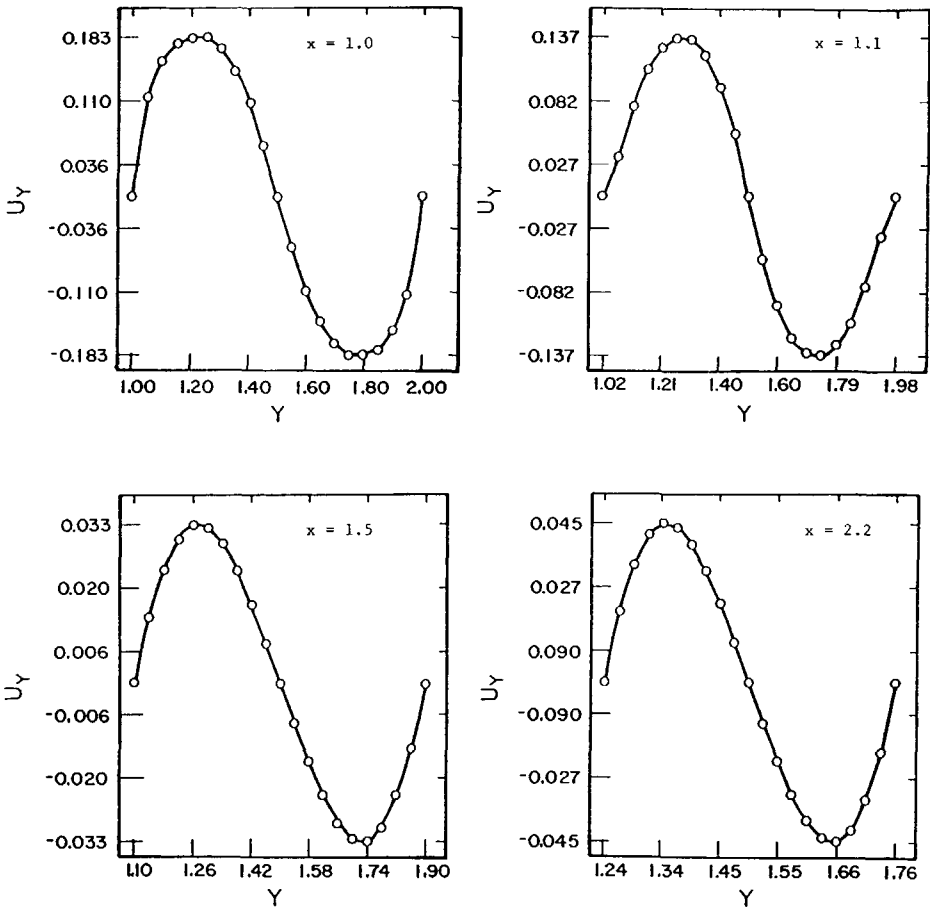
Fig. 4. y-Velocity component profiles at various axial positions in the converging wall geometry for power law flow. $n = 0.75$.

($\alpha = 0$) or the finite value associated with the converging flow (see Fig. 6). In both cases, the fully developed profile occurs at about $x = 1.75$ in complete agreement with our earlier finite-difference calculations.[4] However, in the region of the stream impingement point ($1.0 \leq x \leq 1.35$), differences up to 20% in the velocities obtained by the two schemes were seen. These we attribute both to inaccuracies in the numerical differentiation employed in the finite-difference method and to important effects arising from the nonlinear momentum terms previously neglected. The finite-element method more accurately portrays velocity profile changes in this region where a number of important extensional flow effects also occur.

The influence of the power law parameter, n, on the kinematics and velocity profile development was studied for three different values (0.75, 0.50, 0.25). For $n = 0.75$, the axial development of the velocity profile was found to be qualitatively and quantitatively similar to the pattern illustrated in Figure 2 for Newtonian flow. Figure 4 illustrates the behavior pattern for the
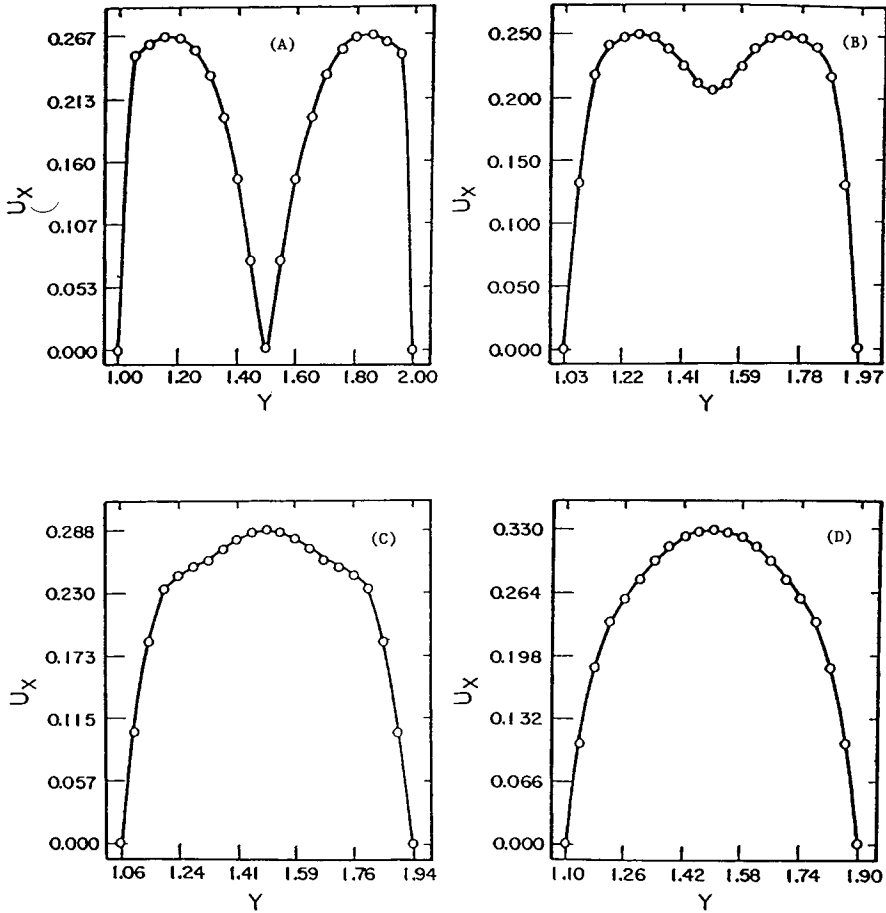
Fig. 5. Velocity distributions for power law flow ($n = 0.25$) in converging wall channel (A) $x = 1.0$; (B) $x = 1.15$; (C) $x = 1.3$; (D) $x = 1.5$.

y-component velocity profile at various axial positions in the converging wall downstream channel. The ratio of the y-velocity to x-velocity maxima drops from a value on the order of 0.6 at the stream impingement point to about 0.06 at $x = 2.2$. This rapid decrease with distance turns out to have an interesting effect on the stress contour shapes in this region as will be shown shortly. The finite magnitude of the y-velocity component also gives a direct measure of the extensional flow generated by the impinging channels geometry. This effect shows more clearly in the profile behavior at lower n as indicated in Figure 5 for $n = 0.25$. Plot (C) shows the presence of a nodule in the centerline region of the parabolic profile resulting from the acceleration of fluid elements along the axis of symmetry caused by the impinging flow. This nodule disappears at $x = 1.5$, plot (D), after which the flattened power law profile for exit flow develops.

Simulations of power law behavior in the straight channel downstream configuration for all three n values showed precisely the same pattern found
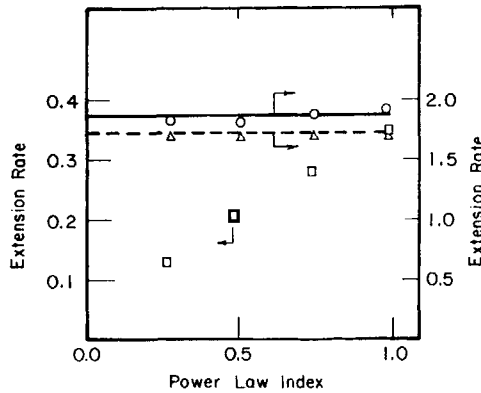
Fig. 6. Nondimensional extension rate versus power law index, n, at the entrance ($\bigcirc$) and exit ($\square$) of the converging wall channel and ($\triangle$) at the entrance of the straight wall channel.

for the Newtonian flow case, that is, a region of strong extensional flow from the bifurcation insert extending downstream to the point where the profile becomes fully developed (i.e., $x = 1.75$). The effects of flow geometry and fluid type on the flow kinematics are summarized in Figure 6 which shows that the extension rate in the exiting region of the converging channel is an increasing function of the power law index [as expected from eq. (8)]. On the other hand, extensional gradients in the strong flow region near the bifurcation insert are seen to be essentially independent of n for both geometries. This latter
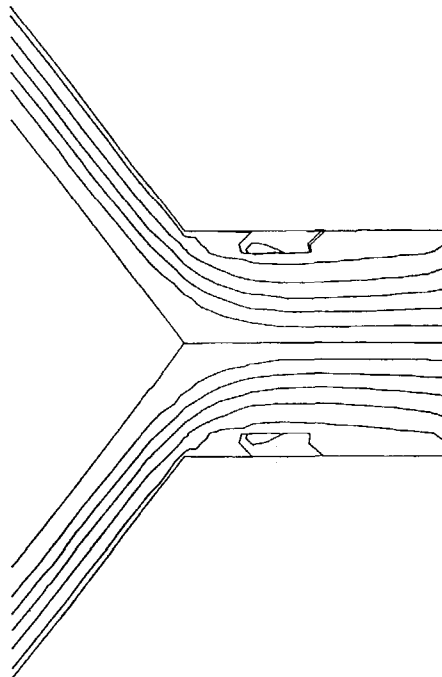

Fig. 7. Streamline pattern for straight channel flow of power law fluid ($n = 0.5$) showing recirculating eddies, Re $= 90$.
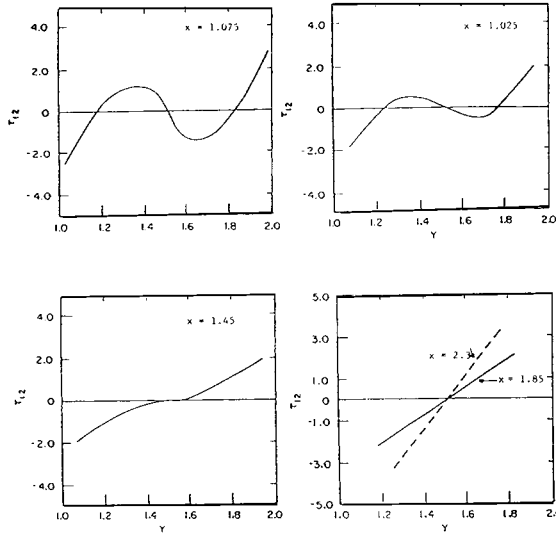
Fig. 8.   Shear stress distribution at various axial positions for power law flow in the converging wall geometry ($n = 0.5$).

pattern, we believe, reflects earlier observations regarding the relative insensitivity of flow kinematics to fluid type in so-called strong, extensional flows.[10-12]

In addition to the increased magnitude and extent of the extensional flow produced in the converging channel geometry, an added practical feature is the reduced tendency for formation of recirculating eddies in the entrance region thus enabling a wider range of accessible, stable flow rates. For example, as seen in Figure 7, circulating eddies are apparent at a Reynolds number of about 90 in the straight channel geometry, while such secondary flow effects were completely absent in the converging geometry for Reynolds numbers in excess of 160 (the upper limit of interest in our processing studies).

Figure 8 shows an example of the developing shear stress distribution for power law flow in the converging channel geometry. The S-shaped profiles in the impinging flow region ($1 \leq x \leq 1.5$) differ considerably from those in conventional converging plate flow[13] and reflect the greater magnitude of the
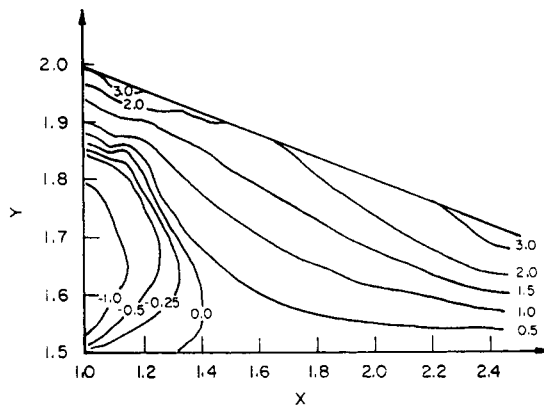

Fig. 9.   Shear stress contours for power law flow ($n = 0.5$) in converging wall geometry.

gradient, $\partial u_y/\partial x$, compared to $\partial u_x/\partial y$ in this region. Beyond $x = 1.75$, $\partial u_y/\partial x$ reduces to that of fully developed converging channel flow resulting in the expected linear stress profile as shown. Essentially the same behavior was seen for Newtonian flow, with the exception that stress levels in general were lower for the power law flows due to the effects of shear thinning.

Figure 9 shows the behavior of the stress contours for power law flow in the converging channel geometry. A knowledge of the unusual shapes of these patterns in the region of stream impingement is essential for the interpretation of birefringence patterns. One sees that for $x > 1.75$, the contours become identical to the straight line patterns associated with converging channel flow, while in the strong flow region $x < 1.75$, both the magnitudes and qualitative shapes are considerably different. The semicircular patterns seen correspond to negative and zero contours resulting from the S-shape of the τ_{xy} component in this region. Generally speaking, the shape of the stress contours in the impinging flow region remained unchanged with n while the magnitudes were slightly lower (i.e., 8% change from $n = 0.75$ to $n = 0.25$).

EXPERIMENTAL

The poly(vinylidene fluoride) used in our studies is manufactured by Solvay, trade name Solef 1010. Complete viscosity and normal stress characterization was carried out over the temperature range of interest (200°C to 220°C) following standard procedures. A cone and plate apparatus (Rheometrics System IV) was used to obtain data in the low shear rate region (10^{-2} $s^{-1} < \dot{\gamma} < 1.2 \ s^{-1}$) and slit or capillary (Haake Buchler Rheocord System 40) devices were used for the intermediate ($1.2 \ s^{-1} < \dot{\gamma} < 10 \ s^{-1}$) and high ($10 \ s^{-1} < \dot{\gamma} < 10^3$) shear rate regions, respectively. Figure 10 shows the viscosity and first normal stress difference (N1) behavior for three temperatures. The linear regions were fit by the power law parameters m and n given in Table I.
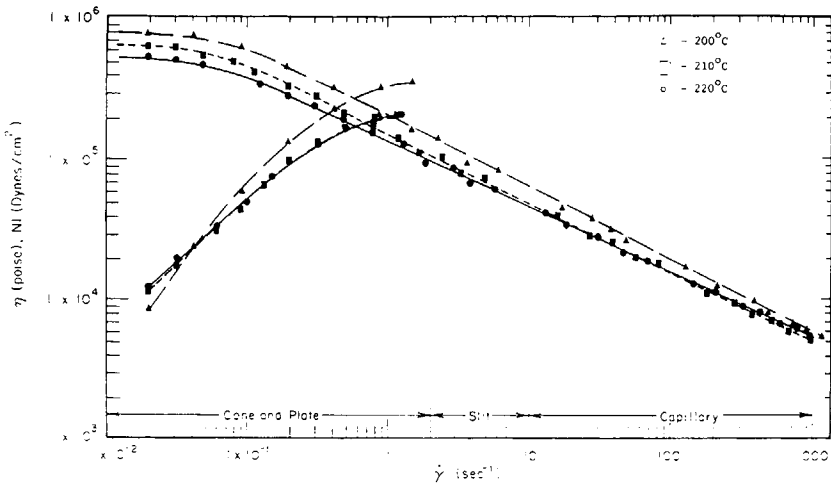

Fig. 10. Viscosity (η), first normal stress difference (N1) behavior of PVF$_2$ for three temperatures ($\triangle$) 200°C; ($\square$) 210°C; ($\bigcirc$) 220°C. Shear rate regions indicate apparatus used for measurement.

TABLE I
Experimentally Determined Rheological Parameters

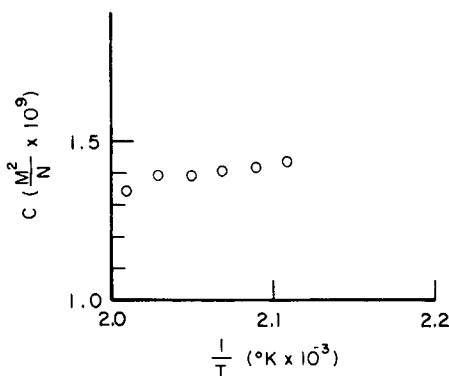| T (°C)	Power law parameter n	Power law parameter m (poise s^{n-1}) $\times 10^{-5}$
220	0.55	1.3
210	0.54	1.5
200	0.46	2.1

Fig. 11.   Stress-optic coefficient of PVF_2 versus inverse absolute temperature. Measurements made in slit-flow die.

Data for the stress-optical coefficient, C, were obtained using a slit-flow device following the procedure discussed in detail in ref. 14. Figure 11 shows a plot of the temperature dependence of C which exhibits the expected trend.[15]*

Figure 12 shows a schematic of the stainless steel die which consists of a straight channel entrance section followed by the bifurcation insert in which the split streams are made to impinge at a 70° (γ) angle followed by a downstream converging flow with $\alpha = 15°$. The minimum aspect ratio at the impingement point is 17 increasing to 86 at the exit. The downstream section was fitted with optical windows to allow viewing of the region corresponding to the bifurcation impingement to a point downstream in the converging flow region. The die was connected to a standard 3/4″ single-screw extruder and extrusion rates equivalent to two-dimensional die flows ranging from 0.01 to 0.03 cm^2/s were studied. Birefringence was measured using a standard plane polariscope configuration consisting of a high intensity light source, filter, achromatic lens, and standard polarizers in rotatable target mounts. Isochromatics were measured under crossed polars and isoclinics were measured from 0° to 90° in 5° increments. Fringe orders were determined by observing the birefringence relaxation after cessation of flow. The procedure used in the analysis is similar to that discussed in ref. 14 and all patterns were recorded on video tape for analysis.

*The exponents tabulated in ref. 14 were incorrectly reported as 10^8. The correct value is 10^9.
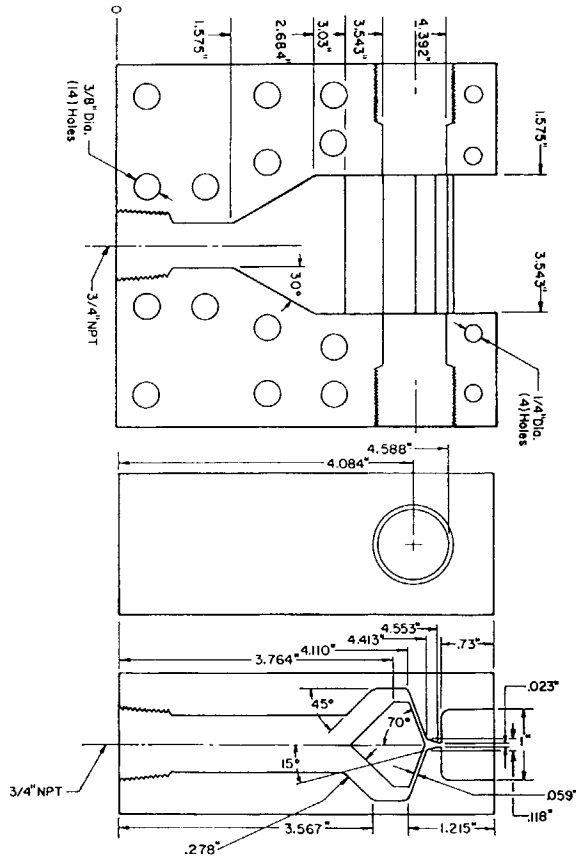
Fig. 12.   Schematic of impinging-converging channels die geometry.

RESULTS AND DISCUSSION

Figure 13 shows a typical example of the isochromatic and isoclinic band patterns for the downstream region which illustrates several of the features shown in our stress contour plots (Fig. 9). In consequence of the changing flow kinematics, both band patterns exhibit a pronounced axial dependence in contrast to the straight line pattern normally observed in converging channel flow.[13,16,17] Both the semicircular and straight line isochromatics are qualitatively in line with our stress contour calculations. One also notes that complete extinction occurs along and near the symmetry axis of flow demonstrating that a strong extensional flow exists in this region from the channel entrance to the exit point. This behavior was found for the entire flow rate range studied and contrasts sharply with that normally seen in a converging plates geometry. There, for example, at flow rates approximately 3 times higher than that in Figure 13, extinction along the centerline only occurs for the last half of the channel,[17] thus the effective extensional flow is confined to the exit region in such geometries. In the present case, as our calculations also show, the impinging channels produce an effective extensional flow over the
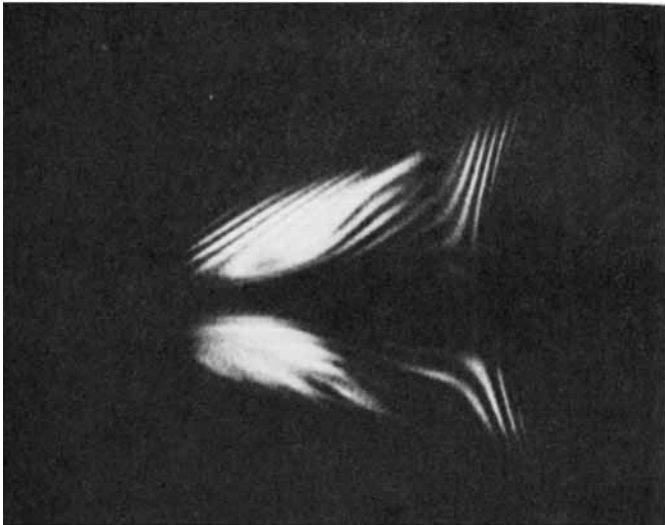
Flow Direction

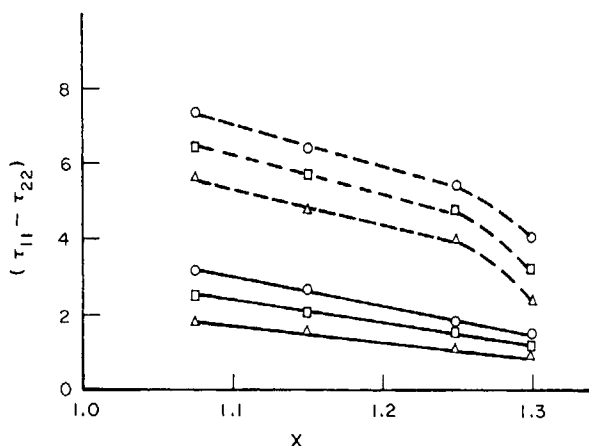Fig. 13. Isochromatic (top) and 80° isoclinic (bottom) patterns for PVF$_2$ at 210°C and $q = 0.02$ cm^2/s.

Fig. 14. Calculated (—) and measured (---) dimensionless first normal stress dependence.
△—0.01 cm²/s; □—0.02 cm²/s; ○—0.3 cm²/s.

entire downstream channel length which is in fact strongest at the tapering entrance.

The maximum magnitudes of the extensional stress occur along the symmetry axis and can be readily obtained from the birefringence, Δn, given a knowledge of the fringe order, N, the optical path length (channel width) L, and the wavelength λ, through the standard relation, $\Delta n = N\lambda/L$. Figure 14 shows a comparison between the observed and calculated dimensionless first normal stress difference which results. Not surprisingly, normal stresses based on the purely viscous power law model underestimate the actual stresses by as much as 300% in the region of highest extensional flow near the insert. This difference decreases as one approaches the fully developed converging flow. However, it is obvious that elastic effects are still quite important. As one moves from the axis of symmetry, the magnitude of the extensional stresses lessens and that of the shearing stresses increases. This is illustrated in Figure 15, which shows the locus of points along the y axis where the magnitude of
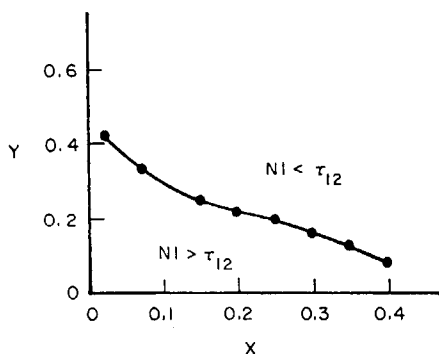

Fig. 15. Comparison of magnitudes of the first normal stress difference, $N1$, and shear stress distributions.
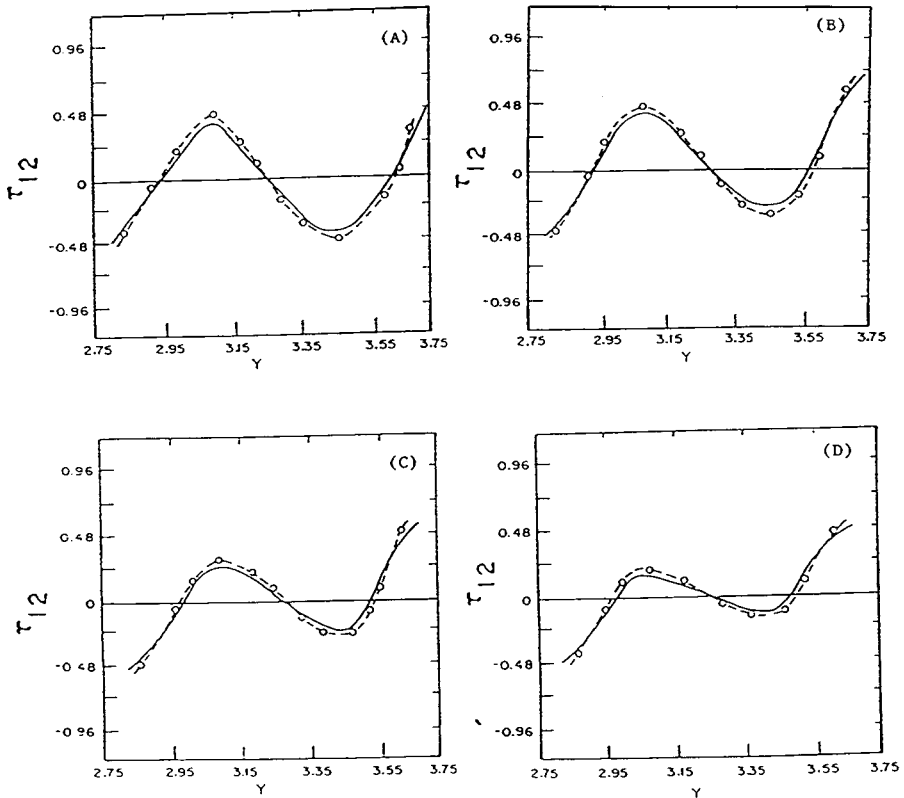
Fig. 16.   Experimental (---) and numerical (—) stress distributions at various axial positions. $T = 210°C$, $q = 0.01$ cm^2/s. (A) $x = 1.075$, (B) $x = 1.15$, (C) $x = 1.25$, (D) $x = 1.3$.

the first normal stress difference exactly equals the shear stress (obtained as indicated below). Below this line, extensional forces become dominant while above it shear forces become dominant. Morphological investigations of quenched extrudates (Part II) demonstrated that, above a critical stress level, chain alignment in the strong flow region is sufficient to cause row-nucleated crystallization and an increased tendency for formation of the β polymorph.

In order to obtain quantitative information on the shear stress distributions, a fine mesh, identical to that used in the finite-element calculations, was superimposed on photographs and values of birefringence (Δn, from the isochromatics) and orientation angle (χ, from the isoclinics) were computed at each node. As is usually the case with confined flows, the isoclinic bands exhibited spreading due to wall effects and therefore measurements for a given χ were made to the edge nearest the symmetry axis.[14] Figures 16–18 show comparisons of experimental and numerical stress distributions (calculated using the appropriate power law parameters) at various positions in the downstream channel for three different flow rates. Profiles near the point of impingement exhibit a characteristic S shape which is reflected in the semicircular nature of the isochromatics (Fig. 13) indicating that a given fringe
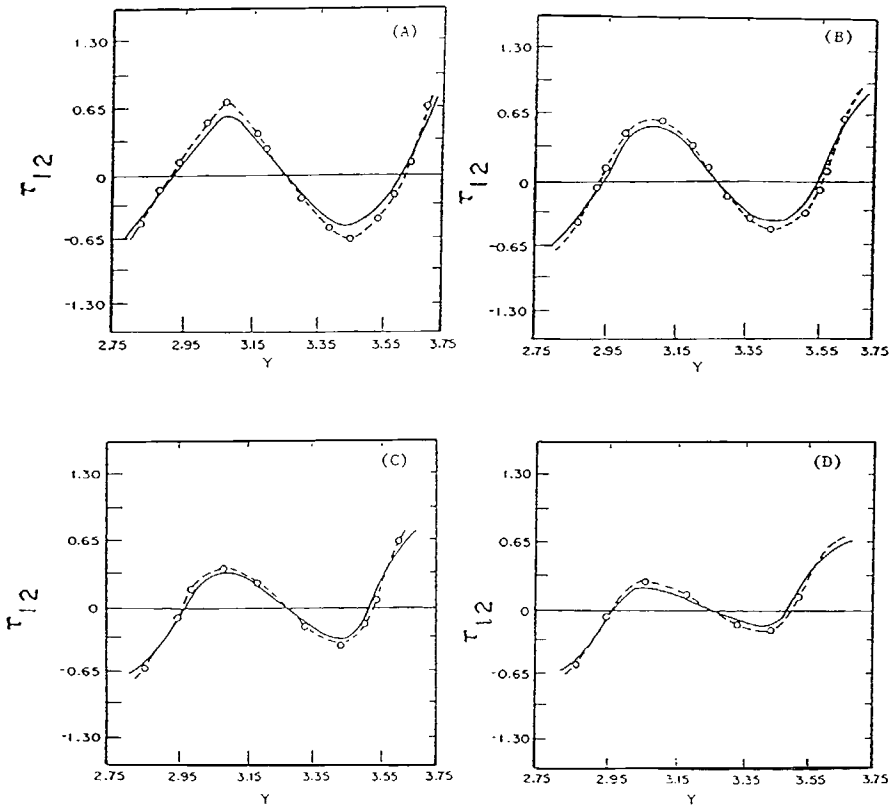
Fig. 17. Comparison of stress distributions for $q = 0.02$ cm^2/s, positions same as noted in Fig. 16.

corresponds to two different orientations. Figure 16, corresponding to the lowest flow rate, shows a surprisingly good agreement between measured and calculated stresses. The difference varies from about 6%, near the insert, to less than 2% near the converging flow exit. Figures 17 and 18 show that the agreement between measured and calculated stresses decreases with increasing flow rate with differences being the most pronounced in the strong extensional flow region near the insert. In all cases measured stresses exceed those based on the purely viscous power law model. This trend is consistent with observations concerning extensional gradients encountered during flows around submerged bodies.[11] In such a case one finds that with increasing Weissenberg number (i.e., elastic effects) and extensional flow strength, both the magnitude and shapes of the stress profiles can be profoundly affected, although streamline shapes remain relatively insensitive to the level of elasticity.[11,12,17] It is noteworthy that in the present case the overall shapes of the shear stress profiles, as well as their qualitative behavior with distance, are well described by the power law model. This result may be inherent in the kinematics imposed by the geometry of the flow cell, that is, as indicated in Figure 15, in the strong flow region shear stresses approach zero by symmetry, or it may reflect an inherently lower elasticity level in our PVF$_2$.
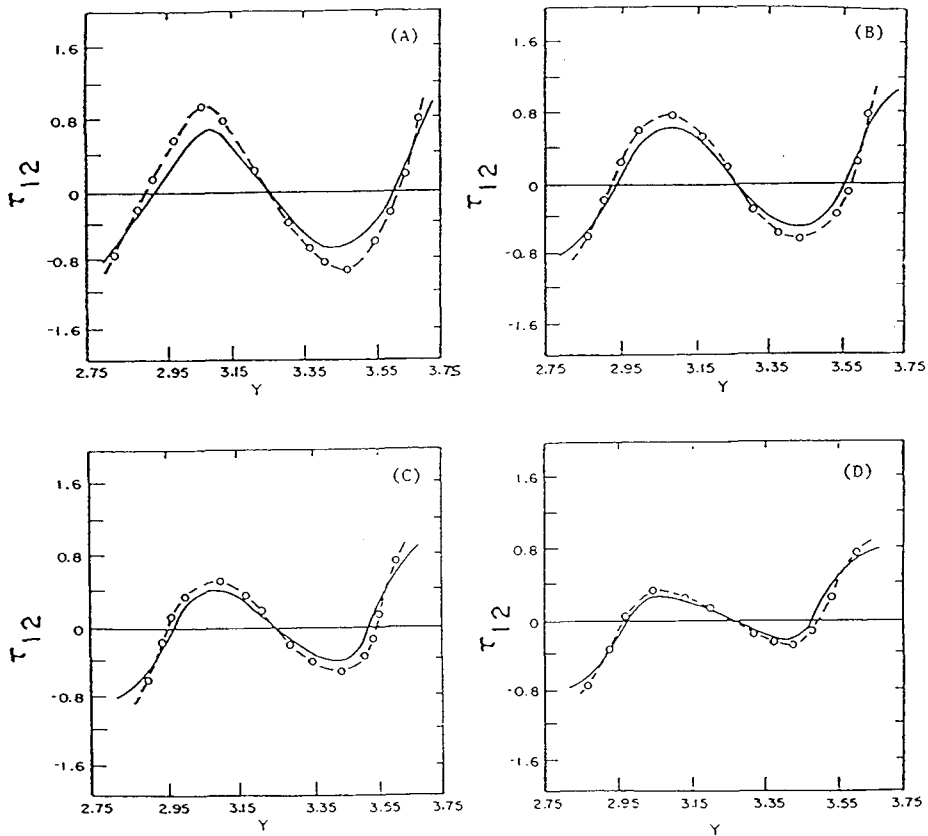
Fig. 18.   Comparison of stress distributions for $q = 0.03$ cm^2/s, positions same as noted in Fig. 16.

CONCLUSIONS

In this article we have presented an analysis of the melt flow history of PVF$_2$ in an extensional flow, film-processing geometry. Our numerical analysis has provided complete flow kinematics and stress behavior for our film geometry as a function of power law parameters and Reynolds number. Our results show that the stress field computed by our power law simulation can qualitatively and reasonably quantitatively describe the shear stress behavior of PVF$_2$ melt in our geometry and that elastic normal stress effects are important near the symmetry axis of flow. As will be discussed in Part II, a knowledge of the stress history is important for the interpretation of the oriented structure formation and polymorphic phase transitions which can be produced in this important material during and after melt processing.

References

1. A. J. Lovinger, in *Developments in Crystalline Polymers*, D. C. Bassett, Ed., Applied Science, London, 1981.

2. W. T. Mead, A. E. Zachariades, T. Shimada, and R. S. Porter, *Macromolecules*, **12**, 473 (1979).

3. T. Shimada, A. E. Zachariades, W. T. Mead, and R. S. Porter, *J. Crystal Growth*, **48**, 334 (1980).

4. B. Khomami and A. J. McHugh, *J. Appl. Polym. Sci.*, **33**, 1495 (1987).

5. R. B. Bird, W. E. Stewart, and E. N. Lightfoot, *Transport Phenomena*, Wiley, New York, 1960, pp. 103 and 108.

6. *FIDAP Users Manual*, Revision 2.0, Fluid Dynamics International, Evanston, IL, 1984.

7. M. Bercouier and M. S. Engleman, *J. Comp. Phys.*, **20**, 181 (1979).

8. T. J. R. Hughes, W. K. Liu, and A. Brooks, *J. Comp. Phys.*, **18**, 30 (1978).

9. B. Khomami, Ph.D. thesis, University of Illinois, Urbana (1987).

10. G. Tiefenbruck and L. G. Leal, *J. Non-Newt. Fluid Mech.*, **10**, 115 (1982).

11. I. S. Dairanieh and A. J. McHugh, *J. Non-Newt. Fluid Mech.*, **19**, 81 (1985).

12. M. E. Mackay and A. J. McHugh, *J. Rheol.*, **29**, 655 (1985).

13. C. D. Han, *Rheology in Polymer Processing*, Academic, New York, 1976.

14. A. J. McHugh, M. E. Mackay, and B. Khomami, *J. Rheol.*, **31**, 619 (1987).

15. A. S. Lodge, *Proc. Fifth Int. Cong. Rheol.*, vol. 4, S. Onogi, Ed., University Park Press, Baltimore, 1970, p. 169.

16. K. C. Liu, M.S. thesis, University of Tennessee, Knoxville (1962).

17. M. E. Mackay, Ph.D. thesis, University of Illinois, Urbana (1985).